Response of different electron beam melting produced Alloy 718 microstructures to thermal post-treatments

(article starts on next page)

Response of different electron beam melting produced Alloy 718 microstructures to thermal post-treatments

Tejas Gundgire[a,*,1], Sneha Goel[a,1], Uta Klement[b], Shrikant Joshi[a]

[a] Department of Engineering Science, University West, 46186 Trollhättan, Sweden
[b] Department of Industrial and Material Science, Chalmers University of Technology, 41296 Gothenburg, Sweden

ABSTRACT

Electron beam melting (EBM) was used to produce Alloy 718 specimens with different microstructures (columnar, equiaxed and a combination thereof) by varying the process parameters. The present study aimed at assessing the response of such varying as-built microstructures to identical thermal post-treatments, which included hot isostatic pressing (HIPing) followed by heat treatment involving solution treatment and aging. The effect of these treatments on defect content, grain structure, hardness and phase constitution in the specimens was specifically analysed. Despite differences in defect content of as-built specimens with distinct microstructures, HIPing was effective in closing defects leading to samples exhibiting similar density. After HIPing, grains with equiaxed morphology or columnar grains with lower aspect ratio showed higher tendency for grain growth in comparison to the columnar grains with higher aspect ratio. The various factors affecting the stability of grains during HIPing of builds with distinct microstructures were investigated. These factors include texture, grain size, and secondary phase particles. The carbide sizes in the different as-built samples varied but were found to be largely unaffected by the post-treatments. Solution treatment following HIPing led to greater precipitation of grain boundary δ phase in regions with coarser grains than the smaller ones. After HIPing and heat treatment, all specimens exhibited similar precipitation of γ″ phase regardless of their grain morphology in the as-built condition.

1. Introduction

Powder bed fusion additive manufacturing (AM) techniques such as electron beam melting (EBM) enable production of near net shaped highly complex geometries in layer by layer fashion using difficult to machine materials like Alloy 718 [1]. Alloy 718 is a precipitate strengthened Ni−Fe based superalloy widely used in aerospace industry due to its excellent properties like high strength, high temperature corrosion resistance, good weldability etc. [2]. Therefore, by virtue of its relevance to numerous actual applications, a growing body of work on the understanding of EBM production of Alloy 718 can be seen from recent reviews on this subject [3–5].

The microstructure of EBM built Alloy 718 is commonly composed of columnar grains elongated along the build direction with preferred ⟨001⟩ orientation [2]. Due to this crystallographic texture the material typically exhibits anisotropic mechanical behaviour [6]. On the other hand, an equiaxed grain structure exhibits isotropic mechanical behaviour which could be beneficial for applications demanding such

properties [2,6]. Consequently, there have been several studies aimed at exploring the possibility of achieving equiaxed grain structure through different approaches using EBM [6–8]. The type of as-built microstructure (from columnar to equiaxed) that can be achieved has been shown to be governed by scan strategy and by manipulating EBM process parameters. For instance, Kirka et al. [6] and Dehoff et al. [9] showed formation of equiaxed grains by changing the scanning strategy from the default raster strategy to point source (multi spot) melting. Helmer et al. [10] also studied equiaxed grain formation by altering the scanning rotation between layers. The intent was to alter the solidification conditions, namely growth rate (R) and thermal gradient (G) at the liquid-solid interface to influence grain morphology via manipulation of the G/R ratio [7,11]. Therefore, the above studies have tried to achieve suitable combinations of G and R which fall within the window for equiaxed grain formation. It is worth mentioning that the range of G/R ratios that result in columnar and equiaxed morphologies is dependent on the material (composition, nuclei density, solidification temperature interval) as elaborated by Kurz et al. [12]. In case of Alloy

718 produced by EBM, G/R ratios for equiaxed and columnar grain formation have been modelled by Raghavan et al. [13].

Despite this improved understanding of formation of the various solidification morphologies in EBM built Alloy 718, there is lack of knowledge about the response of distinct as-built microstructures to thermal post-treatments. The as-built Alloy 718 material is typically exposed to post-treatments comprising hot isostatic pressing (HIPing), and heat treatment (HT) involving solution treatment and aging to take care of concerns related to defects, anisotropy, local formation of un-desirable phases, etc. [14]. There have been several studies on the re-sponse of the typical EBM columnar microstructure to thermal post-treatments [15–17]. However, to the best of authors' knowledge, only Kirka et al. [6,18] have reported the response of fully columnar and fully equiaxed EBM Alloy 718 microstructures to HIPing and HT, and showed that only the equiaxed grains exhibited grain growth after the post-treatment. This was attributed to the lack of pinning precipitates at the grain boundaries in case of equiaxed microstructure [6]. In this context, it is worth mentioning that although for wrought Alloy 718 there is knowledge of response of microstructure (commonly equiaxed) to HT [19], the underlying mechanisms are different than those in AM material [20]. For instance, wrought Alloy 718 microstructure mainly depends on dynamic recrystallization [19] whereas in case of AM Alloy 718 static recrystallization is typically observed after HT [20]. Further, among the AM processes, the factors influencing microstructural sta-bility depend on the nature of the specific processes, as in case of the two leading powder bed fusion processes viz. EBM and laser powder bed fusion (LPBF). For LPBF built Alloy 718, the grain growth during HT is typically attributed to residual stress present in the material [21]. Residual stress in LPBF built Alloy 718 is known to be higher than in EBM material, and is likely a function of processing factors such as cooling rate, preheating, etc. [22]. Therefore, there is a need for a more detailed and quantitative investigation of the various factors particu-larly affecting grain stability in EBM built Alloy 718 with varying as-built microstructures during post-treatment. Thus, the aim of the pre-sent study was to provide further understanding of the response of different EBM Alloy 718 microstructures to identical post-treatments.

In the present study, different electron beam melted Alloy 718 mi-crostructures, produced by varying the EBM processing conditions, were subjected to two thermal post-treatments, namely (a) HIP alone and (b) HIP + ST + A, involving HIPing followed by solution treatment and aging. A systematic investigation of microstructural characteristics such as grain morphology and orientation, defects, phase constitution, as well as hardness analysis of the specimens in as-built and post-treated condition was carried out to ascertain how builds with very distinct as-built microstructures, particularly in terms of grain mor-phology (fully columnar, fully equiaxed and their combinations) re-spond to identical post-treatments.

2. Experimental procedure

2.1. EBM built Alloy 718

The plasma atomized feedstock powder used in the present study had nominal chemical composition as given in Table 1. The powder was supplied by Arcam AB, Sweden and had a nominal particle size in the range of 40–100 μm. The EBM specimens were built in an Arcam A2X EBM machine. In total, 36 cubes each with 20 × 20 × 20 mm di-mension were produced with different process parameters and scanning strategies to tailor the grain structure from the typically observed

columnar structure to equiaxed. Parameters such as spot time, beam current, line offset etc. were varied. It is worth mentioning that the samples studied in the present work were strategically selected, based on their distinct microstructures, from an elaborate design of experi-ments (DOE) designed for achieving wide range of G and R values during EBM processing Alloy 718. Detailed specifications of the DOE in relation to the process parameter window and scanning strategies have been earlier reported elsewhere by the concerned group [23]. Given that the focus of the present study was specifically on evaluating the response of different microstructures to identical post-treatments, four specimens with distinct microstructures (see Fig. 1) were selected from the above set of samples. Table 2 lists the designation and description of the four specimens. For the sake of clarity, it should be pointed out that specimen C-MA(D) had columnar grains with lower (2–4) and higher (> 4) aspect ratios (length/width) at demarcated regions. The micro-structures of the selected specimens have been described in detail later, in Results and discussion section.

2.2. Thermal post-treatments

The four as-built specimens were subjected to two thermal post-treatments namely, HIP and HIP + ST + A. The HIPing treatment, as per the process graph shown in Fig. 2, was performed at Quintus Technologies, Sweden. A hot isostatic press (Model QIH21) was used with Argon as the inert process gas. Parts of the HIPed specimens were further subjected to heat treatment comprising of solution treatment and two step aging, and were labelled as HIP + ST + A. The process parameters during the course of HIPing and ST + A are specified in Table 3. It is worth mentioning that the choice of parameters for HIP and ST was based on the recommendations of ASTM (F3055) standard for post treatment of powder bed fusion produced Alloy 718 [24]. The aging protocol employed in the study corresponds to a shortened cycle compared to the protocol recommended in the above ASTM standard and is based on a recent study carried out in this group with the intent of eventually shrinking the post-treatment schedule for PBF Alloy 718 [25].

2.3. Metallographic preparation and characterization

For microstructural analysis, the specimens were sectioned along the building direction using an aluminium oxide cut-off wheel. The sectioned specimens were hot mounted using a Buehler Simplimet 3000 automatic mounting press. The mounted specimens were ground and polished using a semi-automatic Buehler Ecomet 300 Pro grinder-pol-isher in accordance with the recommended procedures [26]. To reveal some of the microstructural features of interest, the polished specimens were electrolytically etched with oxalic acid-water solution (1:10 ratio) and Kalling's 2 reagent. For each case, a voltage of 2–3 V was applied for 5–10 s. A light optical microscope (LOM) ZEISS AX10 (Zeiss, Ger-many) was used for characterization. Investigation at higher magnifi-cation was carried out using two scanning electron microscopes (SEMs) (Hitachi TM 3000 (Hitachi, Japan) equipped with an energy-dispersive X-ray spectroscopy (EDS) system, and a LEO 1550 Gemini (Zeiss Ger-many) with a field emission gun equipped with an HKL Nordlys EBSD detector from Oxford Instruments, UK). The EBSD data was analysed using HKL Channel 5 software. Defect content (vol%) and amount of carbides (vol%) in the specimens were determined from 15 cross-sec-tion micrographs, using ImageJ software. Micrographs for defect and carbide quantification were taken at 50× and 2500× magnification, respectively. The area fraction and volume fraction were assumed to be equal [27]. For each as-built specimen, the number of grain boundary carbides per unit length of grain boundary was evaluated using 15 micrographs at 2500× magnification. The primary dendritic arm spa-cing (PDAS) in the as-built specimens was measured using the line in-tercept method as employed previously in other reported studies [28,29]. A minimum of 35 dendrites were analysed from SEM

Table 1
Nominal chemical composition of Alloy 718 powder used in this work.

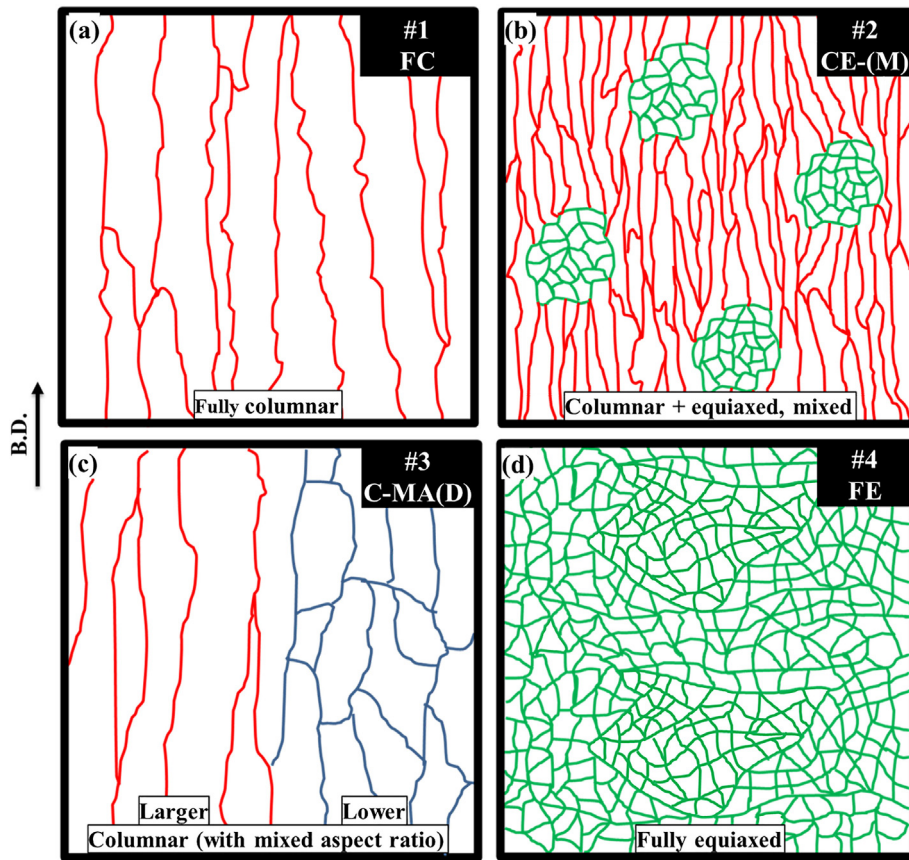| Element	Ni	Cr	Fe	Nb	Mo	Ta	Ti	Al	C
wt%	54.11	19	Bal.	4.97	2.99	< 0.01	1.02	0.52	0.03

Fig. 1. Schematic showing the different grain morphologies of the selected as-built specimens. The arrow on the left indicates building direction.

Table 2

Designation and description of selected specimens with different microstructures.

Specimen	Nomenclature	Microstructure
#1	FC	Fully columnar
#2	CE-(M)	Columnar + equiaxed, mixed
#3	C-MA(D)	Columnar (with mixed aspect ratio), demarcated
#4	FE	Fully equiaxed

Fig. 2. Time-temperature-pressure graphs during HIPing treatment.

micrographs for each specimen. Hardness values of all the specimens were measured using a Shimadzu HMV-2 Vickers microhardness tester, employing a load of 4.9 N applied for 15 s. Twelve readings were recorded over the entire cross-section of the specimens to determine the mean and standard deviation.

Table 3

Post-treatment parameters.

Post-treatment	Parameters
HIP	• 1120 °C/100 MPa/4 h/RC
HIP + ST + A	• HIP: 1120 °C/100 MPa/4 h/RC
	• ST + A
	• Solution treatment: 954 °C/1 h/RC to RT
	• Aging: 740 °C/4 h/FC to 635 °C/1 h/RC to RT

Note: RC and FC denote rapid cooling and furnace cooling, respectively. RT indicates room temperature.

3. Results and discussion

The focus of the present work was on the response of different as-built microstructures, particularly grain morphologies, when subjected to identical post-treatments. Therefore, as-built samples with distinct grain morphologies were carefully selected for detailed investigation in the as-built and post-treated conditions (see Fig. 1 in Section 2), and the ensuing results are presented and discussed in this section. The comprehensive microstructural investigation involved characterization of grain morphology, grain orientation, defects, phase distribution and quantification, and microhardness.

3.1. Characteristics of as-built specimens

3.1.1. Defects

The defects observed in EBM built Alloy 718 can be classified as process induced and powder induced defects [5]. The LOM micrographs of defects observed in as-built specimens are shown in Fig. 3. The variation in defect content in the different as-built samples was in the range of 0.13% to 0.84% as ascertained from image analysis and
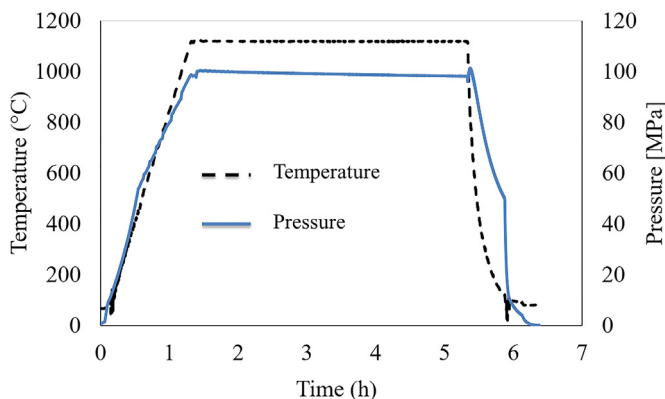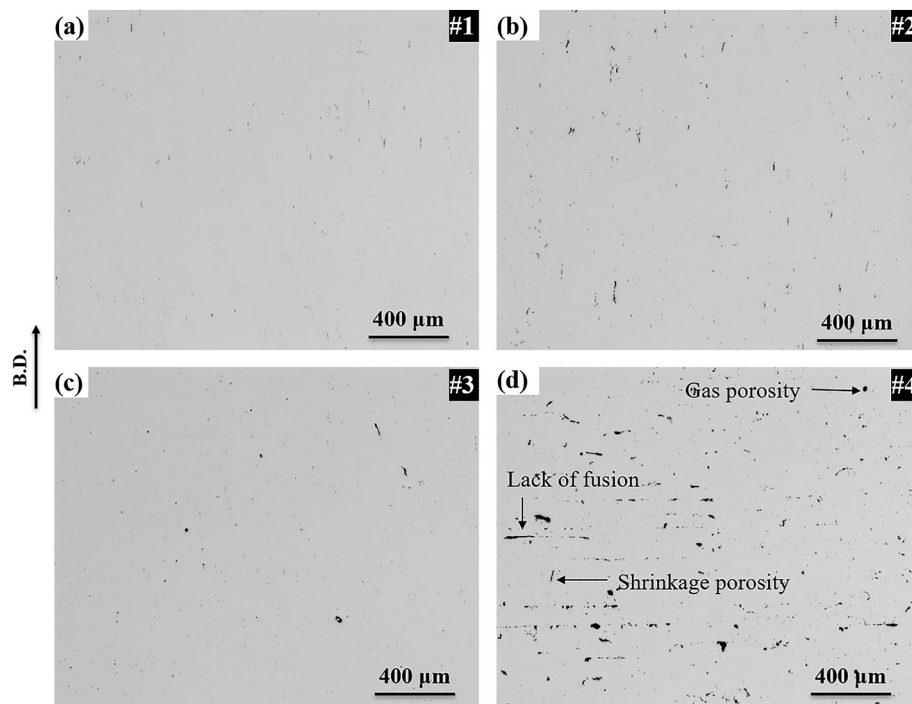
Fig. 3. LOM micrographs showing defects in as-built condition: (a) Specimen #1 (FC), (b) Specimen #2 (CE-(M)), (c) Specimen #3 (C-MA(D)) and (d) Specimen #4 (FE). The arrow on the left indicates building direction.

reflected in the quantification results later depicted in Fig. 8. The process induced defects include lack of fusion and shrinkage porosities which are perpendicular and parallel to the building direction, respectively. The powder induced defects include gas pores formed due to entrapped gas in the powder. The reasons for the formation of all these defects have been elaborated previously [5].

3.1.2. Grain structure

The four selected specimens, designated as described previously in Table 2, exhibited the following distinct grain morphologies: (a) fully columnar (#1, FC), (b) columnar and equiaxed in mixed fashion (#2, CE-(M)), (c) columnar (with mixed aspect ratio) at demarcated regions (#3, C-MA(D)), and (d) fully equiaxed (#4, FE) as shown in Fig. 4. It is worth mentioning that the columnar grains parallel to the build direction as seen in sample #1 are typically observed in EBM built Alloy 718. It has been previously reported that a columnar microstructure typically exhibits anisotropic tensile behaviour whereas an equiaxed microstructure shows an isotropic response [6]. In this study, distinct microstructures ranging from fully columnar and to completely equiaxed were achieved by manipulating spot melting strategies and systematically varying other process parameters as described in a previous publication [23]. For tailoring the grain structure (from columnar to equiaxed), the main idea was to achieve varying combinations of G and R inside the melt pool such that the solidification conditions fall within the desired window as illustrated in Fig. 4(e). The solidification conditions indicated in Fig. 4(e) were qualitatively assessed from the observed microstructure. The relative cooling rates in the various samples were mainly estimated by the carbide sizes as described in Section 3.1.3. These results were further corroborated by the PDAS for the columnar microstructure in samples #1 and #3 as stated in Section 3.1.3. It should be noted that Fig. 4(e) seeks to merely position the different specimens on a G-R map based on the observed microstructures and approximate qualitative estimation of cooling rates.

3.1.3. Phase constitution
3.1.3.1. Carbides. White blocky particles were observed in all the specimens at high magnification and, from the SEM-EDS analysis,

these were identified to be NbC type primary carbides. The amount of these carbides was quantified, and the results are shown in Fig. 5(a). A more careful examination revealed differences in the carbide content and sizes in the various as-built specimens as shown in Fig. 5(a) and (b). Although not shown in the figure for the sake of brevity, the amount and size of carbides in the distinct regions of sample #3 (C-MA(D)) were observed to be similar. Sample #1 (FC) and #2 (CE-(M)) had relatively smaller sized carbides compared to sample #3 (C-MA(D)) and #4 (FE). The size of the primary carbides, which form during solidification [31], can be influenced by the cooling rate. In cast Alloy 718, Mitchell [31] has reported that increase in cooling rate caused decrease in carbide size. Therefore, as the carbide sizes in the samples appeared to be in the following order: #1, #2 < #4 < #3 as depicted in Fig. 5(b), the relative cooling rates can be estimated to be: #1, #2 > #4 > #3.

The cooling rate can also be estimated from the PDAS as stated by Kirka et al. [32] and Karimi et al. [33] but only in case of columnar microstructure. The PDAS values are inversely related to the cooling rates as experimentally observed in case of cast Alloy 718 [34]. Therefore, PDAS was measured for the samples with columnar grain structure [35], i.e., specimen #1 and #3 and was qualitatively related to the cooling rate. It is worth mentioning that, for cooling rate estimation, only the primary dendrites observed in the last solidified layers, i.e. at the top of the specimens, were analysed, similar to the analysis done by Kirka et al. [32]. The PDAS in specimen #1 (FC) was 17 μm, and ~34 μm in specimen #3 (C-MA(D) (similar value for regions with low and high aspect ratio of columnar grains) as visualized in Fig. 6(b) and (d), which indicates slower cooling rate in sample #3. Moreover, presence of well-developed secondary dendrites and extensive segregation in specimen #3, shown in Fig. 6(d), further supports the above observation. It can be inferred that the slow cooling in specimen #3 (C-MA(D)) could have caused formation of larger carbides in comparison to specimen #1 (FC), as visualized in Fig. 6(a) and (c). Hence, from the carbide size and PDAS the following order of cooling rate can be expected: #1, #2 > #4 > #3. In this context, it is pertinent to note that for a given grain morphology, the cooling rate can determine the grain size (GxR) as illustrated in Fig. 4(e). While the size of the equiaxed
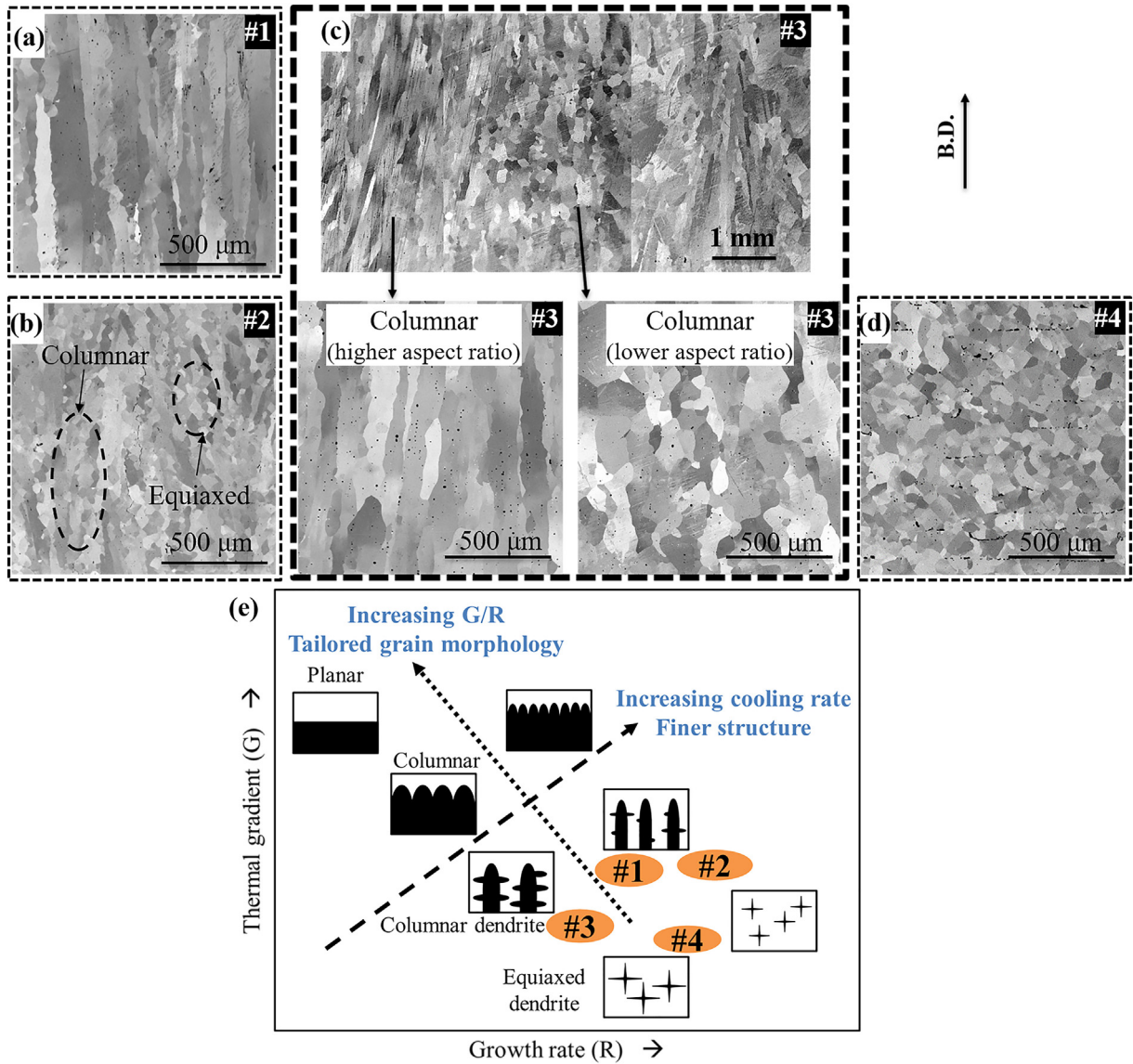
Fig. 4. SEM micrographs in back-scattered electron (BSE) mode showing the various as-built microstructures: (a) fully columnar in Specimen #1 (FC), (b) mixed columnar and equiaxed in Specimen #2 (CE-(M)), (c) columnar (with mixed aspect ratio) at demarcated regions in Specimen #3 (C-MA(D)), and (d) fully equiaxed in Specimen #4 (FE). The arrow on the top right indicates building direction. In (e), the qualitative effect of G and R on the solidification morphology and size is illustrated, with the indicated conditions for each sample; figure inspired from [30].
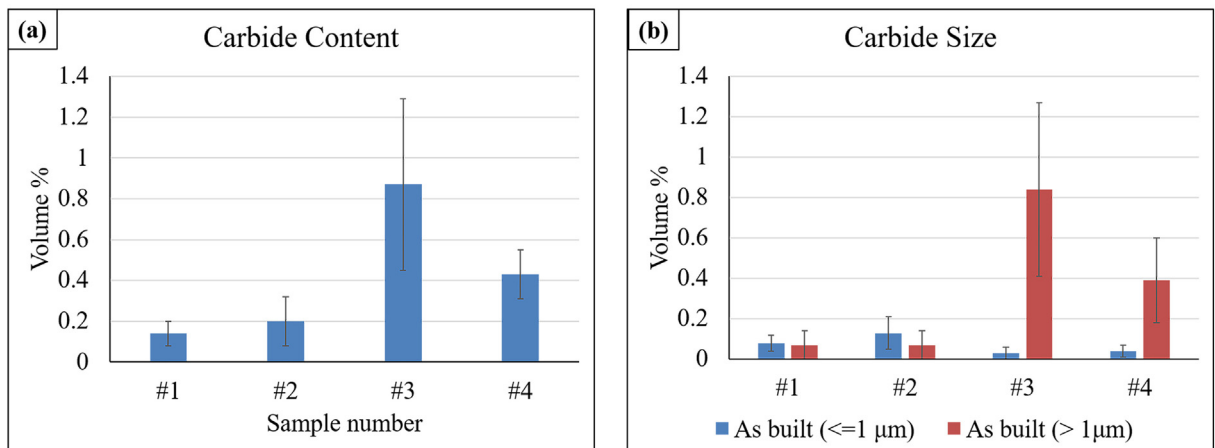
Fig. 5. Quantification of (a) carbide content and (b) carbide size in various as-built specimens.

Carbide   Dendrite   Cooling rate
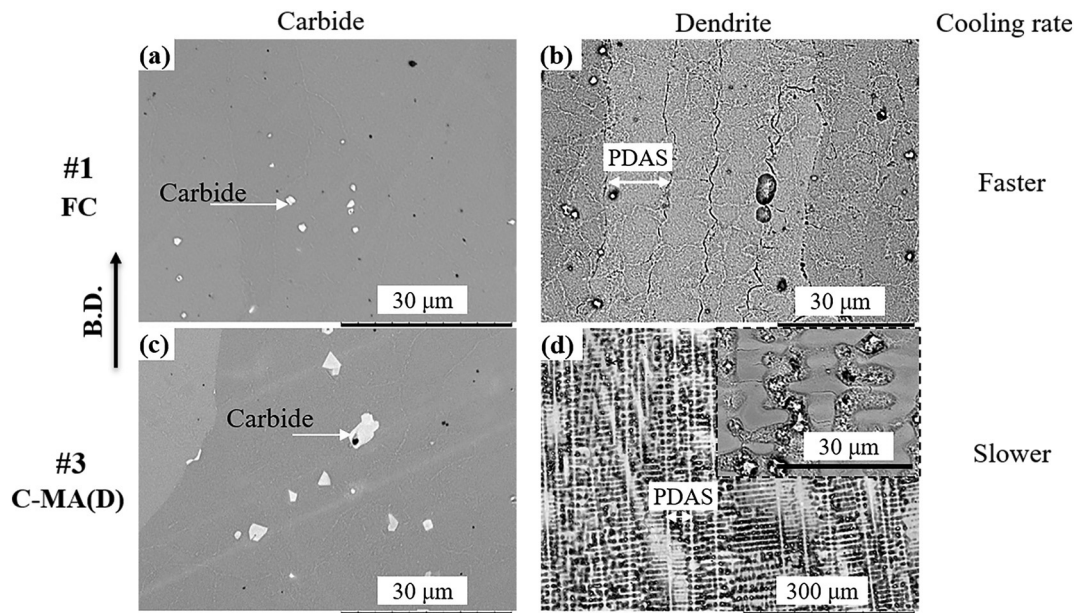
Fig. 6. SEM-BSE micrographs showing the relation between carbide size and relative cooling rate as indicated by primary dendritic arm spacing in Specimen #1 (a–b), and Specimen #3 (c–d); the inset in (d) shows interdendritic segregation. The arrow indicates building direction.

grains [36] in the specimens appears to be in the following order: #2 < #4 (refer Fig. 4), the width of the columnar grains [15] in the specimens appears to be: #2 < #1 < #3. Therefore, the grain sizes/ widths corroborate well with the above-mentioned relative cooling rates estimated using carbide size and PDAS values.

3.1.3.2. Delta phase. In addition to blocky carbides, in all the four as-built specimens, bright network-like features were observed when using back-scattered electron (BSE) mode for imaging. At higher magnification these network-like features were discerned to be composed of fine intragranular δ phase precipitates of size in the range of 60–100 nm. For the purpose of illustration, these δ phase particles are shown for specimen #1 (FC) and #4 (FE) in Fig. 7. Such stacked appearance of δ phase particles forming a network has also been previously observed by Kirka et al. [32]. A clear image of

intergranular δ phase is also shown in the inset of Fig. 7(d).

3.2. Effect of thermal post-treatments

3.2.1. Defects

All the defects present in the specimens (stated in Section 3.1.1) were quantified to evaluate the total defect content in the specimens. The as-built specimens exhibited defect content in the range of 0.13% to 0.84%. Subjecting the specimens to HIPing led to reduction in amount of defects by an order of magnitude (down to 0.02%–0.05%) as shown in Fig. 8(a), and subsequent heat treatment (ST + A) led to no further significant changes in the defect content. Fig. 8(b), (c) and (d) show micrographs revealing defect distribution in as-built, HIP and HIP + ST + A conditions, respectively in case of sample #4 (FC). It can be seen from the figure that the defect content in the as-built sample #4
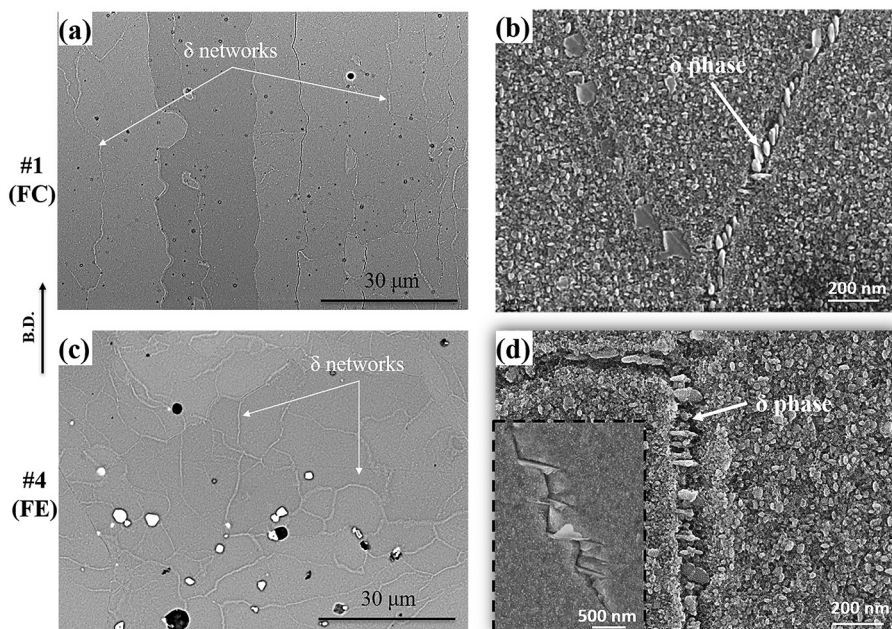
Fig. 7. SEM micrographs in as-built condition showing intragranular bright network-like features at lower magnification, which were composed of stacked δ phase particles discerned at higher magnification, for Specimen #1 (FC) (a–b) and Specimen #4 (FE) (c–d); the inset in (d) shows grain boundary δ phase. The arrow indicates the building direction.
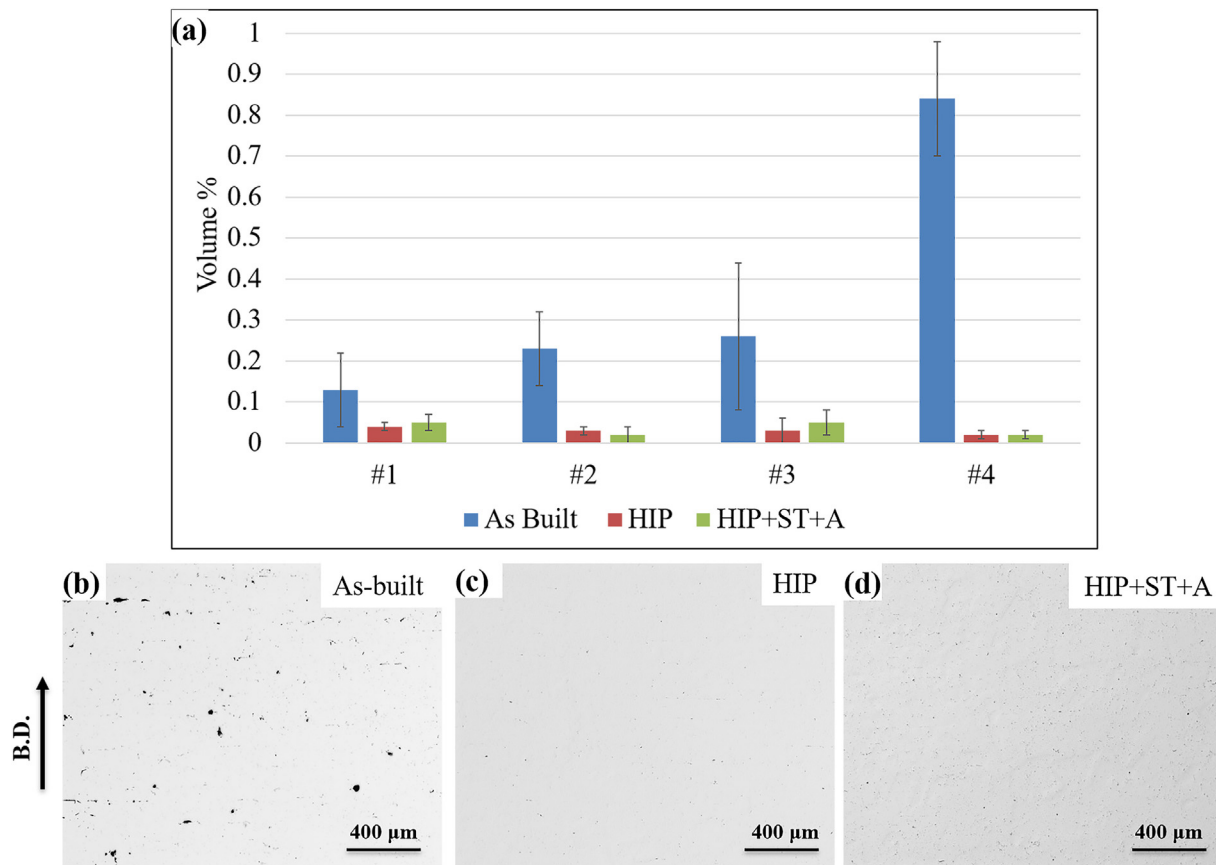
Fig. 8. Defect content in as-built, HIP and HIP + ST + A conditions (a), and LOM micrographs showing defects in Specimen #4 in as-built (b), HIP (c), and HIP + ST + A (d) conditions. The arrow indicates building direction.

(FC), with the majority of defects being lack of fusion type, was distinctly higher than the other specimens. As previously shown in Fig. 4(d), this specimen exhibited a fully equiaxed microstructure. Given the above observation and as previously hypothesized by Polonsky et al. [37], it can be inferred that the lack of fusion defects could have assisted formation of equiaxed grains, since the defects can potentially hinder epitaxial growth from the base material due to local variation in heat flux which can, in turn, alter the G (thermal gradient) and R (growth rate) values.

3.2.2. Grain structure

The effect of HIP and HIP + ST + A treatments on grain size and grain morphology was similar in all cases as shown in Fig. 9. It is acknowledged that the grains are three-dimensional, and in the present work the examination has been done only in one direction (building direction) as carried out in most previous studies [6,10,13]. It should also be mentioned that when the microstructure was viewed in other directions, as exemplified in the Supplementary data file, consistent information was obtained. In the present study, the grain width of the fully columnar specimen #1 (FC) remained largely unaffected by HIPing (1120 °C for 4 h) as shown in Fig. 9(a–c). Here grain width is assessed because of the large length of the grains. Specimen #2 (CE-(M)) did not undergo any evident grain growth in either the columnar or the equiaxed region after HIPing as shown in Fig. 9(d–f). However, in specimen #3 (C-MA(D)) although no evident change in columnar grains with large aspect ratio (greater than 4) was observed after HIPing (see Fig. 9(g–i)), the columnar grains with lower aspect ratio (nearly 2–4) showed significant grain coarsening as seen in Fig. 9(j–l). Similarly, in specimen #4 (FE) with fully equiaxed grains (aspect ratio ≤ 2), abnormal grain growth was observed after HIPing as shown in Fig. 9(m–o). All the factors responsible for grain growth, i.e., texture,

grain morphology, grain size, and secondary phase particles are discussed below. Moreover, given that ST + A had no evident further effect on the grain structures, only the as-built and HIPed specimens were further investigated to determine the operating mechanisms behind grain growth.

EBSD analysis was carried out to investigate grain size and orientation distribution to get further insight into the reason(s) responsible for the observed grain growth characteristics in the different as-built microstructures. It is worth mentioning that the driving force for grain growth during thermal post-treatment is the reduction of free energy associated with the grain boundaries, and the extent of grain growth is governed by several other factors such as misorientation, grain size, grain boundary pinning particles, etc.

Specimen #1 (FC) did not undergo any evident change in grain width after HIPing, as evident from the EBSD results given in Fig. 10(a–b), reaffirming the findings already discussed in Fig. 9. This can be attributed to several reasons: a) presence of strong texture, b) large grain size, and c) carbides pinning the grain boundaries. The strong texture noted in Fig. 9(a) implies decreased driving force for grain growth [38]. In addition, compared to the equiaxed grains (as discussed later), the columnar grains have larger grain size. Moreover, the significant number of carbides (normalized by grain boundary length) at the grain boundaries as given in Fig. 11(d) and visualized in Fig. 11(e) could have also hindered grain growth by Zener pinning. Kirka et al. [6] have also reported lack of grain growth after HIPing of textured columnar grains due to pinning of grain boundaries by carbide particles. During Zener pinning, the second phase particles attached to the moving boundary exert a pulling force on the boundary, thereby restricting its motion. In case of heat treated LPBF Alloy 718, Chlebus et al. [20] have visualized this pinning effect. In this context, it is pertinent to note that, although curvature of grain boundaries involving
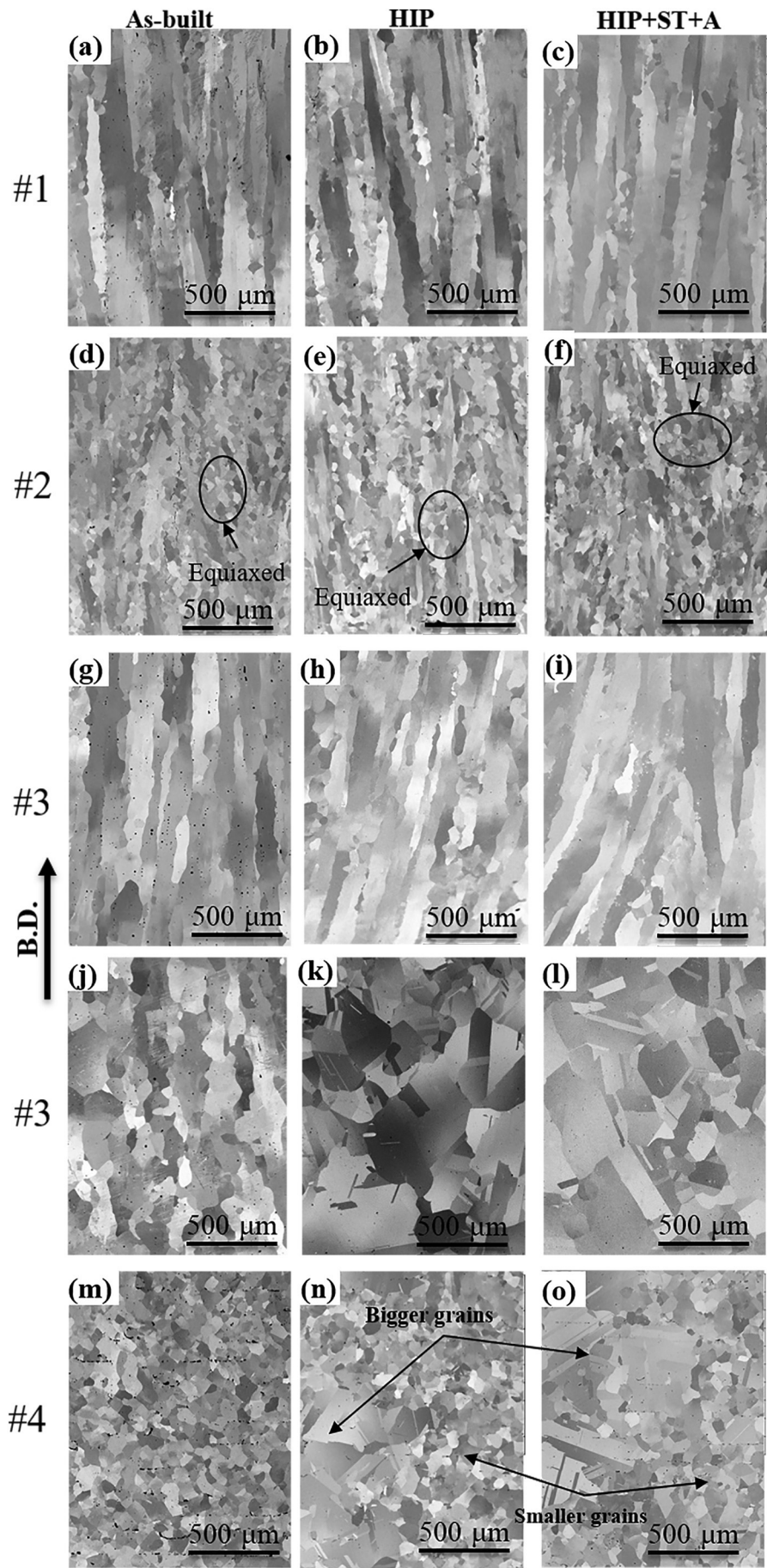
(caption on next page)

Fig. 9. SEM-BSE micrographs in as-built, HIP and HIP + ST + A conditions for all specimens: (a–b–c) Specimen #1 (FC), (d-e-f) Specimen #2 (CE-(M)), (g–h–i) columnar region (with higher aspect ratio) in Specimen #3 (C-MA(D)), (j–k–l) columnar region (with lower aspect ratio) of Specimen #3, and (m–n–o) Specimen #4 (FE). The arrow indicates the building direction.

analysis in the transverse direction was not investigated in the present study, prior work has shown that this could also influence grain growth [20].

The highly textured columnar grains in specimen #2 (CE-(M)) did not exhibit any observable change in grain width after HIPing, as shown in Fig. 10(c–d), for similar reasons as noted for specimen #1 (FC). The large number of grain boundary carbides in specimen #2 could have inhibited grain growth. The fact that there is no evident grain growth observed in the equiaxed locations of specimen #2 (CE-(M)), despite the random texture and small grain size, can be attributed to both the presence of large number of carbides at the grain boundaries and restriction to growth imposed by the surrounding columnar grains (see inset in Fig. 10(c)). However in specimen #3 (C-MA(D)), after HIPing, recrystallization and grain growth in columnar grains with lower aspect ratio, as shown in Fig. 10(g), was mainly attributable to the relatively

weaker texture in the as-built condition, refer Fig. 10(h). Recrystallization after HIPing was noted by the significant change in shape (appearing equiaxed) and orientation of the grains. On the other hand, in the same sample, the columnar grains having higher aspect ratio and strong texture remained largely unaffected after HIPing, as observed in Fig. 10(e) and (f).

In case of specimen #4 (FE), a combination of random texture in the as-built condition (seen in Fig. 10(i)), small grain size, and the low number of carbides at the grain boundaries (later shown in Fig. 11(d)) could have led to the grain growth observed after HIPing as shown in Fig. 10(j). Moreover, the nature of grain growth can be called abnormal grain growth as shown in the inset in Fig. 10(j). Abnormal grain growth occurs due to preferential growth of few grains having a growth advantage over the surrounding grains, leading to grains with varied sizes being developed [38]. Previously Watson et al. [39] reported grain
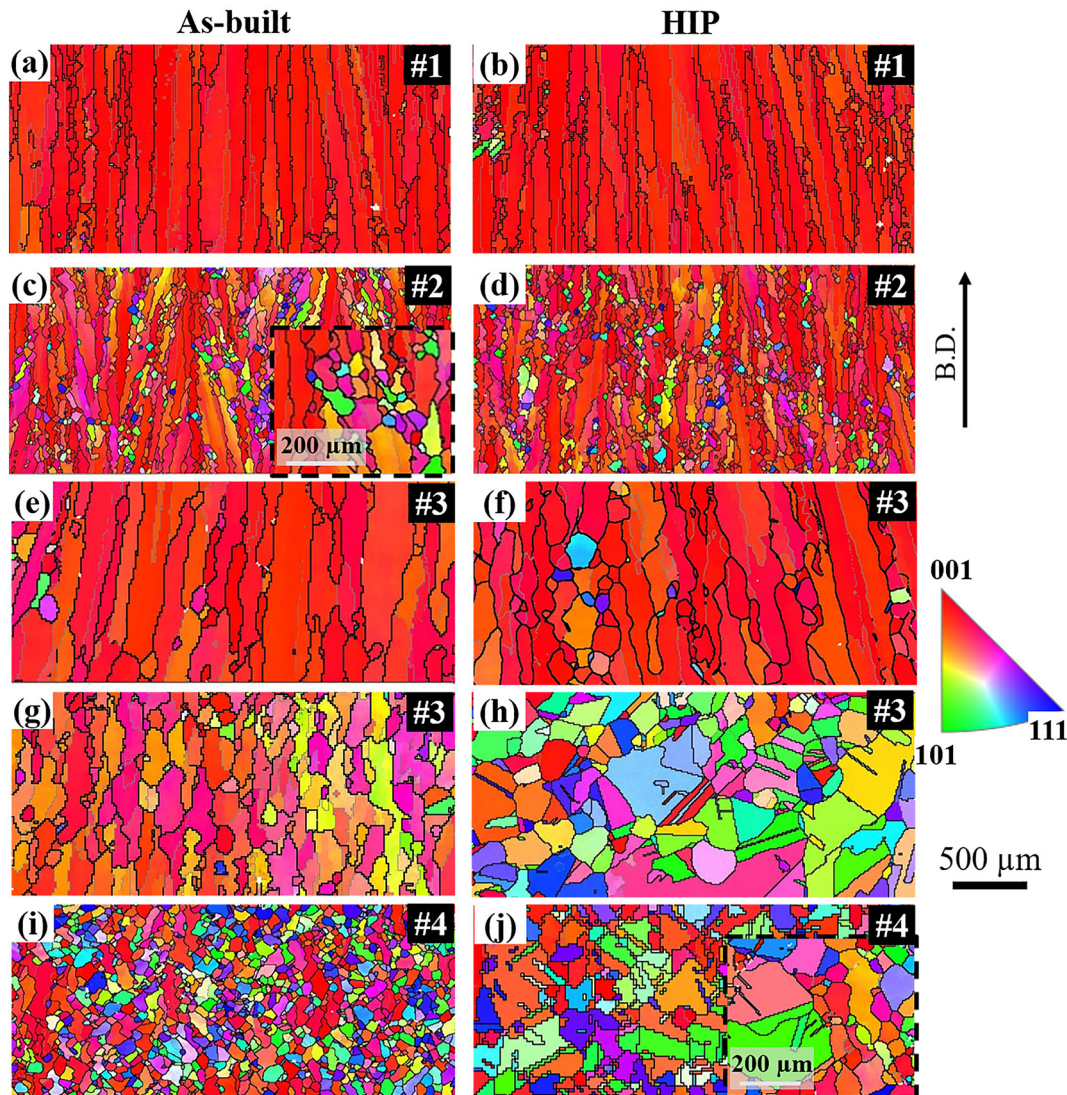
Fig. 10. EBSD orientation maps of the specimens in the as-built and HIPed conditions: (a–b) Specimen #1 (FC), (c–d) Specimen #2 (CE-(M)), (e–f) Specimen #3 (C-MA(D), columnar grains with higher aspect ratio), (g–h) Specimen #3 (C-MA(D), columnar grains with lower aspect ratio), and (i–j) #4 (FC). The maps are given in inverse pole figure colouring with respect to the build direction, indicated by the arrow, with the corresponding colour code provided. Low angle grain boundaries (misorientation 3–10°) and high angle grain boundaries (misorientation > 10°) represented by grey and black lines, respectively. (For interpretation of the references to colour in this figure legend, the reader is referred to the web version of this article.)
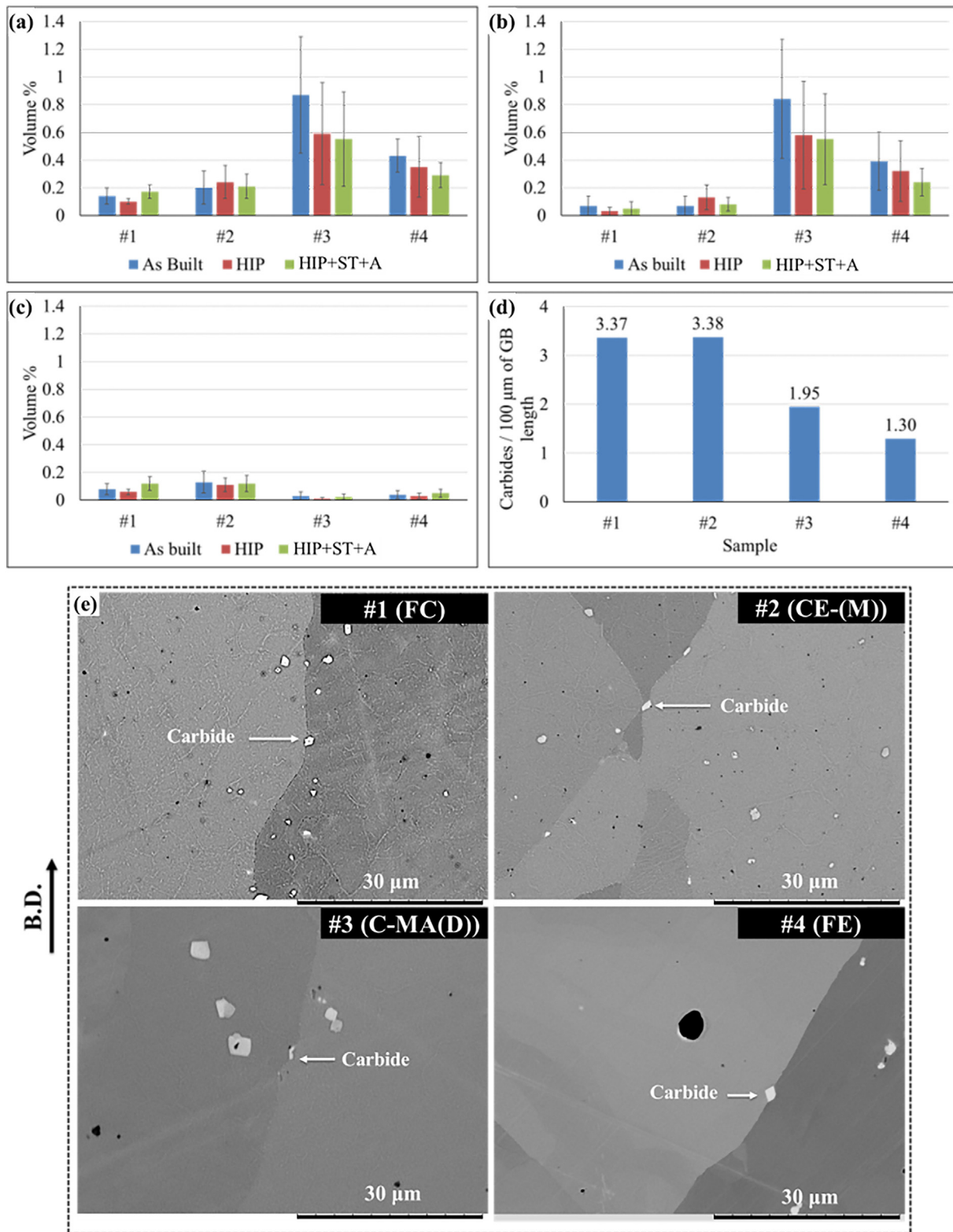
Fig. 11. Comparison of specimens in as-built, HIP and HIP + ST + A condition in respect of total carbide content (a), carbides with diameter > 1 μm (b), carbides with diameter ≤ 1 μm (c); (d) number of grain boundary (GB) carbides per unit length of GB and their (e) visualization (bright features) in the as-built specimens.

growth from 10 to 20 μm to 100–120 μm as abnormal for Alloy 718 during high temperature forging. Bozzolo et al. [40] have used a similar terminology to describe grain growth (from 5 to 30 μm to 90–120 μm) during thermomechanical forming of nickel based superalloys. In the present work, the equiaxed grains in sample #4 had grown from 10–100 μm to 50–400 μm during HIPing. Moreover, high twin density

was observed in the abnormally grown regions in comparison to the other grains, as visualized in Fig. 9(n–o). The above authors have also reported similar response in abnormally grown grains in Alloy 718. The specific mechanism responsible for abnormal grain growth in the present case is not known; however, possible reasons could be non-uniform dissolution of grain boundary pinning δ phase (refer inset in Fig. 7(d))

As-built   **HIP**
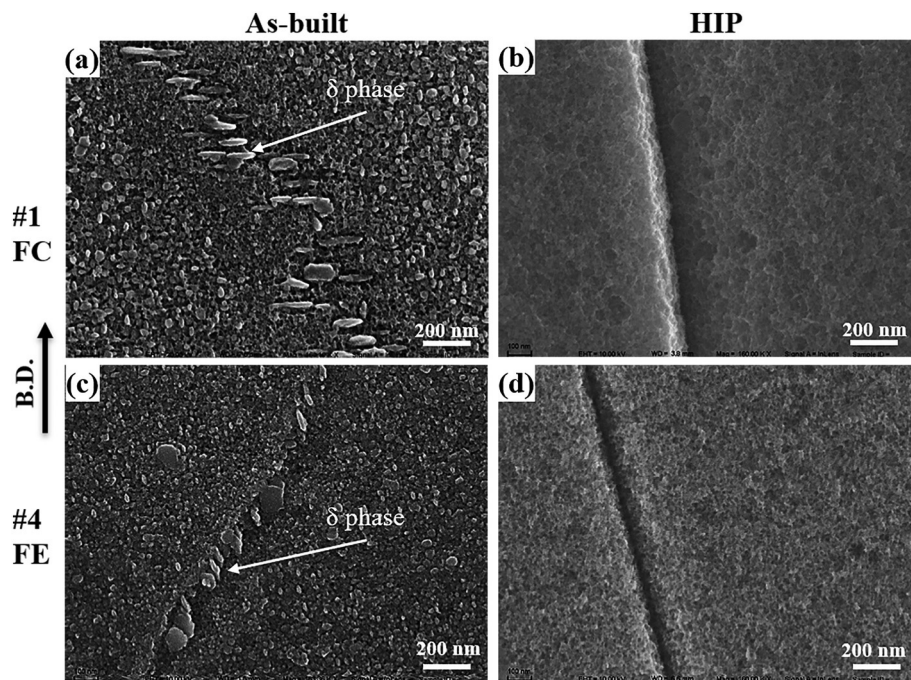
Fig. 12. SEM micrographs showing δ phase present in Specimen #1 (FC) and Specimen #4 (FE) in as-built condition (a, c), but absent in HIPed condition (b, d). The arrow indicates the building direction.

and irregular distribution of carbide particles, as shown in Fig. 11(e). Moreover, it is pertinent to note that the grain size of the grown grains was approximately in the range of 50–400 μm, which is larger than the typical grain size observed in wrought Alloy 718 in post-treated condition, i.e., nearly 10–30 μm [27,41].

Overall, the columnar grains (with strong texture) appeared to resist grain growth, whereas the equiaxed grains (with weaker or random texture) exhibited significant grain growth. Kirka et al. [6] have also reported higher tendency for growth of equiaxed grains. However, that study was restricted to only fully columnar and fully equiaxed microstructure. In the present work, the microstructure with mixed equiaxed and columnar grains showed no evident grain coarsening (sample #2, CE-(M)), as the growth of equiaxed grains was restricted by the surrounding columnar grains. The samples/regions exhibiting grain growth were invariably associated with annealing twins as seen in Fig. 10(h) and (j). Annealing twins are formed during grain migration and its density is dependent on grain size, velocity of grain boundary migration, annealing parameters, grain boundary energy, and stacking fault energy [20,42]. Due to the reduced stacking-fault energy of Nickel at high temperature (40 mJ/m^2 at 1000 °C), twining can likely occur during grain growth in Alloy 718 as previously reported for heat treated LPBF material [20]. It is also worth mentioning that the microstructures which exhibited grain growth after HIPing contained a wide range of grain sizes in the as-built condition, which is a necessary (although not sufficient) condition for any possible grain growth [43].

3.2.3. Phase constitution
3.2.3.1. Carbides.
The total content and size of the carbides remained largely unaffected after both the post-treatments, i.e. HIP and HIP + ST + A as shown in Fig. 11(a), (b) and (c). Therefore, no observable Ostwald ripening of carbides was observed in any of the specimens. This can be attributed to the temperatures used for these post-treatments (maximum of 1120 °C) which were lower than the temperatures at which Ostwald ripening has been previously observed in LPBF produced Alloy 718 (after HIPing at 1160 °C) [44]. Moreover, Ostwald ripening in wrought Alloy 718 has also been reported to occur after heat treatment at 1150–1191 °C [45]. It is worth mentioning that, in the above study on LPBF built Alloy 718, grain growth was observed

after HIPing, which was attributed to dissolution of carbides (which can pin the grain boundaries) during Ostwald ripening [44]. However, in the present study this does not seem to be the prevailing mechanism. Another important concern is the effect of carbides on the properties of Alloy 718. It has been previously discussed that the grain boundary carbides can be beneficial in restricting grain growth during post-treatment [6,15]. However, some prior studies have suggested that carbides noted in EBM-built microstructures have detrimental effect on the mechanical behaviour [2,18]. Therefore, this aspect requires further detailed investigation.

3.2.3.2. Delta phase.
The δ phase (networks) present in the as-built material were completely dissolved after HIPing as seen in the SEM micrographs for specimen #1 (FC) and #4 (FE) given in Fig. 12. Similar behaviour was observed in all other HIPed specimens. Therefore, it can be inferred that HIPing resulted in increased microstructural homogeneity. The complete dissolution of δ phase after HIPing can be attributed to the HIPing temperature of 1120 °C (for 4 h), which is above the δ solvus temperature (~1000 °C [46]). It pertinent to note that, δ phase, if present at grain boundaries, is known to pin grain boundary movement during HIPing [15]. Although not reported specifically for EBM Alloy 718, prior work on a homogenous ingot of Alloy 718 has also shown complete dissolution of delta phase within 10 min at 1100 °C [47] and this is relevant considering that the HIP treatment protocol in the present study was 1120 °C/4 h/100 MPa. Therefore, as aforementioned, the grain growth observed after HIPing was also influenced by other factors.

Although the δ phase was dissolved after HIPing, HIP + ST + A led to re-precipitation of the δ phase particularly at the grain boundaries in all the specimens. This was attributed to the solution treatment step involved during the latter. This observation is in accordance with transformation-time-temperature diagram of Alloy 718 [48]. The grain boundary δ phase in specimen #1 (FC) is shown in Fig. 13(a), and for specimen #2 (CE-(M)) in Fig. 13(b, c). As evident from comparison Fig. 13(b) and (c), there was no significant difference in grain boundary δ phase precipitation in columnar and equiaxed regions. The HIP + ST + A specimen #3 (C-MA(D)) showed higher amount of grain boundary δ phase precipitates in the columnar region than in the
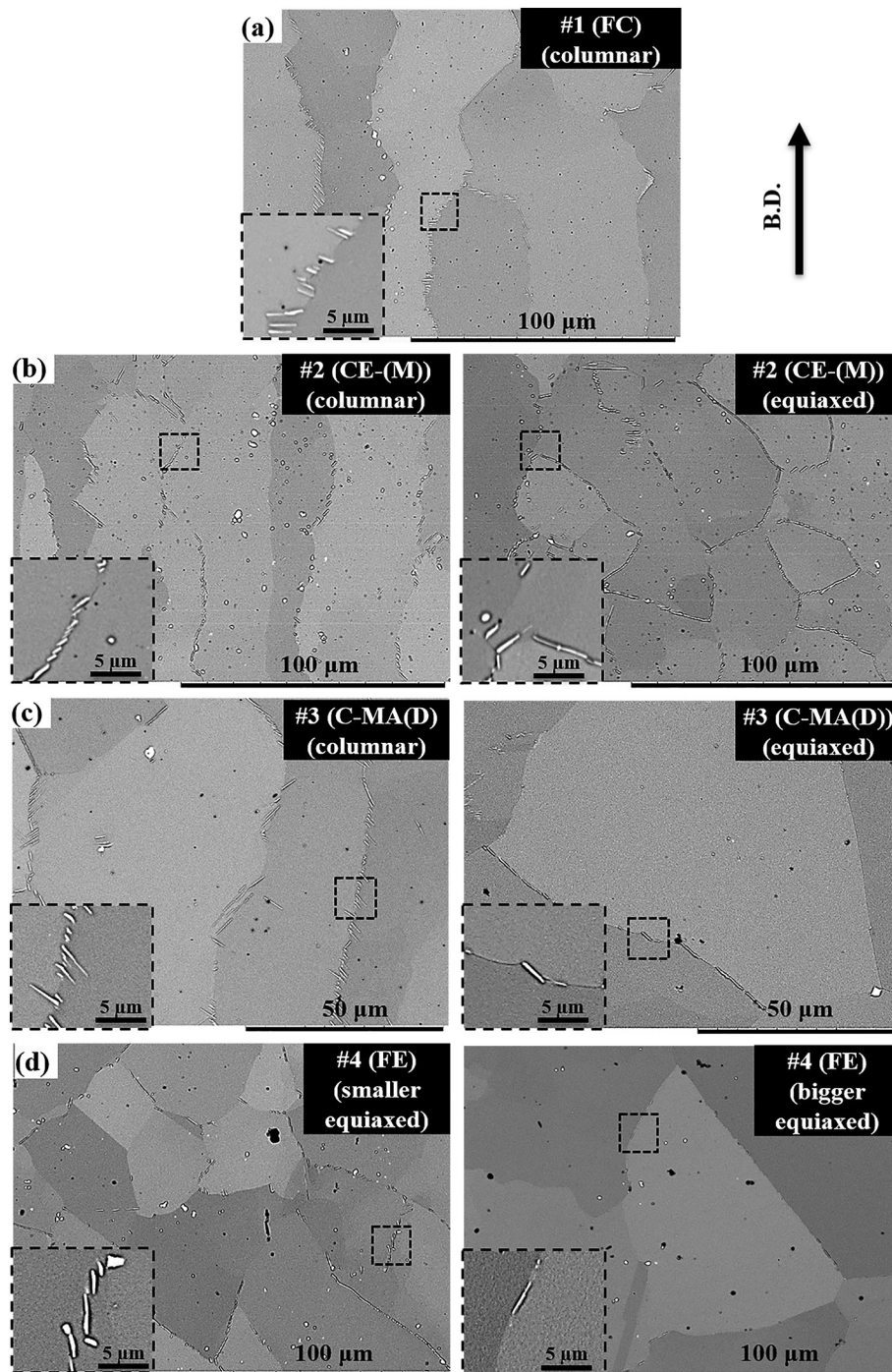
Fig. 13. SEM-BSE micrographs showing grain boundary δ phase precipitates observed after HIP + ST + A in all the investigated specimens at indication locations. The insets clearly reveal δ phase at higher magnification. The arrow indicates the building direction.

equiaxed region, as seen in Fig. 13(d, e). Subjecting the specimen #3 to HIP resulted in recrystallization and significant growth in columnar grains with lower aspect ratio (changed into equiaxed), whereas columnar grains with high aspect ratio were relatively stable. Therefore, it can be inferred that less grain boundary area was available in the equiaxed region compared to the columnar region for precipitation of δ phase during the ST. Less grain boundary area results in slower nucleation kinetics for δ phase precipitation as previously observed in cast Alloy 718 [49]. Moreover, the increase in diffusion lengths (for Nb) with increase in grain size might reduce the δ phase precipitation at the grain boundaries. Specimen #4 (FE), which exhibited abnormal grain growth after HIP, with distinct regions with smaller and bigger grains

also showed similar behaviour. The smaller grain region contained more grain boundary δ phase compared to the bigger grain region, as shown in Fig. 13(f, g), which can be understood by the difference in the amount of grain boundary area available for precipitation. In this context it is worth mentioning that, the effect of δ phase on the mechanical behaviour should be further studied as the reports in the literature have been diverse. For instance, Li et al. [50] have shown the region surrounding grain boundary δ phase to be depleted of γ″ phase, and have proposed that this can relieve stress concentration at grain boundaries and hence improve intergranular crack propagation resistance during creep testing. On the other hand, Valle et al. [51] observed decrease in ductility with increase in δ phase content, while
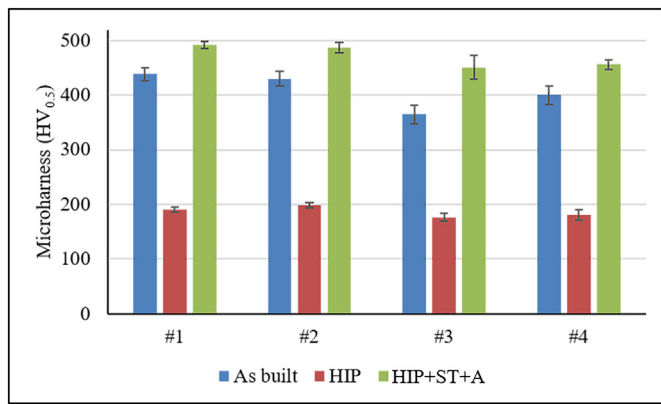
Fig. 14. Microhardness values of all specimens in as-built, HIP and HIP + ST + A conditions.

Deng et al. [2] found no effect of grain boundary δ phase on the tensile properties of EBM built Alloy 718.

3.2.4. Microhardness

The average Vickers microhardness values of as-built, HIP, and HIP + ST + A specimens are depicted in Fig. 14. The microhardness values of all the as-built specimens were higher than the recommended minimum hardness of 350 HV as per AMS 5662 for Alloy 718 [52]. The as-built specimens exhibited slight differences in hardness values as reflected in Fig. 14. In this context, it is worth mentioning that the hardness of the precipitation strengthened Alloy 718 can be described by:

$$H_{total} = H_{matrix} + H_{ps}$$

where H_{total} denotes the total hardness, H_{matrix} represents the intrinsic hardness of the matrix and H_{ps} arising from the precipitation strengthening [53]. The hardness of the matrix is attributable to the solid solution strengthening. The precipitate strengthening mechanisms applicable for Alloy 718, as previously elaborated by Chaturvedi et al. [54], are: (a) order strengthening and (b) coherency strain strengthening. Moreover, it has further been reported that coherency strain strengthening by γ″ (Ni₃Nb) provides the major contribution to the H_{ps}

in Alloy 718 as detailed by Devaux et al. [55]. It should also be mentioned that grain size can also influence hardness as previously elaborated for LPBF Alloy 718 [56].

The noted variation in the hardness of the different as-built microstructures may be attributed to differences in total carbide content among the specimens. For example, specimen #3 (C-MA(D)) which had the highest carbide content (Fig. 11(a)) exhibited the lowest hardness (Fig. 14) and specimen #1 (FC) which had the lowest carbide content showed the highest hardness value. It has been previously reported that the excessive precipitation of these Nb-rich carbides can overconsume Nb from the matrix which is vital for precipitation of the strengthening γ″ phase [57].

Subjecting the specimens to HIPing caused significant reduction in hardness for all the specimens. This can be attributed to dissolution of the strengthening γ″ phase, given that its solvus temperature (~900 °C [58]) is significantly lower than the HIPing temperature of 1120 °C. Henceforth, hardness in the HIPed condition can be attributed to solid solution strengthening which is expected to be the same in all the cases due to homogenization after HIPing. However, the hardness was recovered after HIP + ST + A to values higher than 400 HV in all the samples. This increase in hardness is attributed to the involved systematic aging treatment which was applied to re-precipitate large amount of the γ″ phase visualized in Fig. 15. Among the various HIP + ST + A specimens, no significant differences in the γ″ phase of the specimens could be discerned by the high-resolution SEM micrographs. The slight difference in hardness of the various HIP + ST + A specimens followed a similar trend as observed among the as-built specimens. The exact reason for this behaviour is not known. However, a previous study on wrought Alloy 718 has shown that hardness might vary with grain size, with a decrease in hardness being noted with increase in grain size [56]. Although not discernible through high resolution SEM investigation, given the higher carbide content in HIP + ST + A samples #3 and #4, it can be inferred that lesser Nb was available in the matrix to form γ″ phase during aging treatment in comparison to samples #1 and #2, thereby resulting in lower hardness.

4. Summary and conclusions

The response of very distinct EBM Alloy 718 microstructures to identical thermal post-treatments (HIP, HIP + ST + A) was analysed.
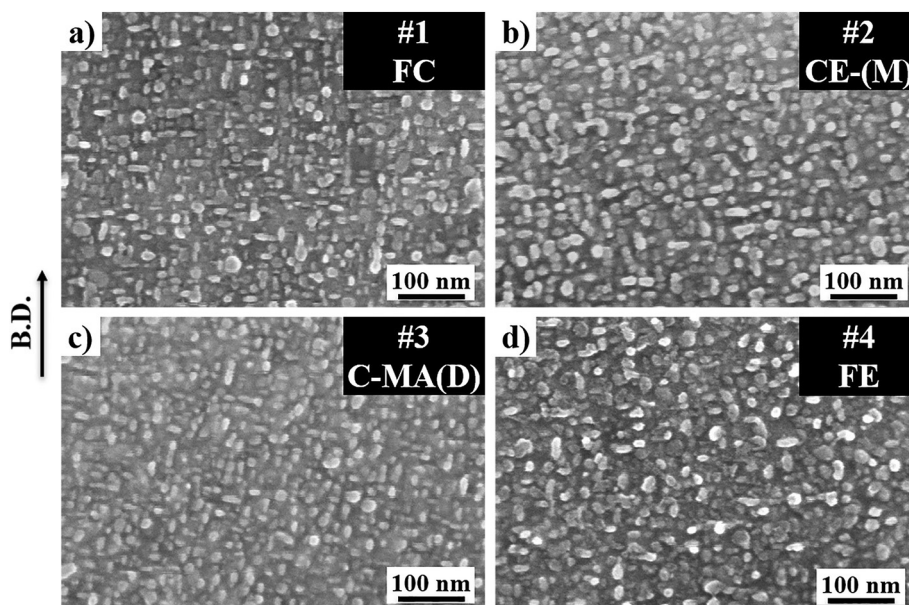

Fig. 15. High resolution SEM micrographs showing the strengthening phase (mainly γ″) in HIP + ST + A specimens: a) Specimen #1 (FC), b) Specimen #2 (CE-(M)), c) Specimen #3 (C-MA(D)), d) Specimen #4 (FE). The arrow indicates the building direction.

Specifically, specimens with four different grain morphologies (columnar, equiaxed and two different combination thereof) were studied. The detailed microstructural investigations presented in this study led to the following findings:

- After HIPing, all the distinct specimens exhibited similar increased density irrespective of the differences in the as-built condition.
- The grain morphology in the as-built condition considerably influenced the grain size resulting after HIPing. The equiaxed and columnar (lower aspect ratio) microstructure exhibited a clear tendency for gain growth, whereas the columnar (higher aspect ratio) microstructure appeared to resist grain coarsening. This behaviour was also related to differences in texture, grain size, and secondary phase particles present in the as-built condition.
- The carbide sizes in the different as-built samples varied and this could be rationalized by the differences in cooling rates during solidification of the samples, with larger carbides associated with slower cooling rates. These carbides were, however, largely unaffected by the post-treatments.
- The δ phase dissolved during HIPing was re-precipitated particularly at the grain boundaries during the subsequent solution treatment step of HIP + ST + A. Greater amount of δ phase precipitation was observed in regions with smaller grains. This was attributed to relatively larger grain boundary area available for precipitation to occur in smaller grain regions, thereby resulting in faster nucleation kinetics for precipitation.
- After HIP + ST + A, all the distinct specimens exhibited similar precipitation of γ″ phase.

Supplementary data to this article can be found online at https://doi.org/10.1016/j.matchar.2020.110498.

Declaration of competing interest

The authors declare that they have no known competing financial interests or personal relationships that could have appeared to influence the work reported in this paper.

Acknowledgements

Author contributions

The authors Mr. Tejas Gundgire and Miss. Sneha Goel have equally contributed to this work, performed all the experimental investigations, analysed all the results, and both had the main responsibility in writing the article. Co-authors Mr. Shrikant Joshi and Ms. Uta Klement have contributed in defining the problem, planning the experimental approach, reviewing analysis of the results, and finalizing the manuscript.

Data availability

The raw/processed data required to reproduce these findings cannot be shared at this time due to technical or time limitations.

References

[1] D. Deng, Additively Manufactured Inconel 718: Microstructures and Mechanical Properties, Licentiate Thesis Linköping University, 2018, https://doi.org/10.3384/

lic.diva-144491.

[2] D. Deng, J. Moverare, R.L. Peng, H. Söderberg, Microstructure and anisotropic mechanical properties of EBM manufactured Inconel 718 and effects of post heat treatments, Mater. Sci. Eng. A. 693 (2017) 151–163, https://doi.org/10.1016/j.msea.2017.03.085.

[3] M. Galati, L. Iuliano, A literature review of powder-based electron beam melting focusing on numerical simulations, Addit. Manuf. 19 (2018) 1–20, https://doi.org/10.1016/J.ADDMA.2017.11.001.

[4] C. Körner, Additive manufacturing of metallic components by selective electron beam melting — a review, Int. Mater. Rev. 61 (2016) 361–377, https://doi.org/10.1080/09506608.2016.1176289.

[5] W.J. Sames, F.A. List, S. Pannala, R.R. Dehoff, S.S. Babu, The metallurgy and processing science of metal additive manufacturing, Int. Mater. Rev. 61 (2016) 315–360, https://doi.org/10.1080/09506608.2015.1116649.

[6] M.M. Kirka, Y.S. Lee, D.A. Greeley, A. Okello, M.J. Goin, M.T. Pearce, R.R. Dehoff, Strategy for texture management in metals additive manufacturing, JOM. 69 (2017) 523–531, https://doi.org/10.1007/s11837-017-2264-3.

[7] R.R. Dehoff, M.M. Kirka, F.A. List, K.A. Unocic, W.J. Sames, F.A. List Iii, K.A. Unocic, W.J. Sames, F.A. List, K.A. Unocic, W.J. Sames, Crystallographic texture engineering through novel melt strategies via electron beam melting: Inconel 718, Mater. Sci. Technol. 31 (2015) 939–944, https://doi.org/10.1179/1743284714Y.0000000697.

[8] B. Shassere, D. Greeley, A. Okello, M. Kirka, P. Nandwana, R. Dehoff, Correlation of microstructure to creep response of hot isostatically pressed and aged electron beam melted Inconel 718, Metall. Mater. Trans. A. 49 (2018) 5107–5117, https://doi.org/10.1007/s11661-018-4812-z.

[9] R.R. Dehoff, M.M. Kirka, W.J. Sames, H. Bilheux, A.S. Tremsin, L.E. Lowe, S.S. Babu, Site specific control of crystallographic grain orientation through electron beam additive manufacturing, Mater. Sci. Technol. 31 (2015) 931–938, https://doi.org/10.1179/1743284714Y.0000000734.

[10] C. Körner, H. Helmer, A. Bauereiß, R.F. Singer, Tailoring the grain structure of IN718 during selective electron beam melting, 2nd Eur. Symp. Superalloys Their Appl, 2014, pp. 1–6, , https://doi.org/10.1051/matecconf/20141408001.

[11] Y. Lee, M. Nordin, S.S. Babu, D.F. Farson, Effect of fluid convection on dendrite arm spacing in laser deposition, Metall. Mater. Trans. B. 45B (2014) 1520–1529, https://doi.org/10.1007/s11663-014-0054-7.

[12] W. Kurz, C. Bezençon, M. Gäumann, C. Bezenc Ëon, M.G. Èumann, Columnar to equiaxed transition in solidification processing, Sci. Technol. Adv. Mater. 2 (2001) 185–191, https://doi.org/10.1016/S1468-6996(01)00047-X.

[13] N. Raghavan, R. Dehoff, S. Pannala, S. Simunovic, M. Kirka, J. Turner, N. Carlson, S.S. Babu, Numerical modeling of heat-transfer and the influence of process parameters on tailoring the grain morphology of IN718 in electron beam additive manufacturing, Acta Mater. 112 (2016) 303–314, https://doi.org/10.1016/j.actamat.2016.03.063.

[14] S. Goel, J. Olsson, M. Ahlfors, U. Klement, S. Joshi, The effect of location and post-treatment on the microstructure of EBM-built Alloy 718, in: E. Ott, X. Liu, J. Andersson, Z. Bi, K. Bockenstedt, I. Dempster, J. Groh, K. Heck, P. Jablonski, M. Kaplan, D. Nagahama, C. Sudbrack (Eds.), Proc. 9th Int. Symp. Superalloy 718 Deriv. Energy, Aerospace, Ind. Appl., The Minerals, Metals & Materials Series, Pittsburgh, USA, 2018, pp. 115–129, , https://doi.org/10.1007/978-3-319-89480-5_6.

[15] P. Nandwana, M. Kirka, A. Okello, R. Dehoff, Electron beam melting of Inconel 718: effects of processing and post-processing, Mater. Sci. Technol. 34 (2018) 612–619, https://doi.org/10.1080/02670836.2018.1424379.

[16] Y.-L. Kuo, A. Kamigaichi, K. Kakehi, Characterization of Ni-based superalloy built by selective laser melting and electron beam melting, Metall. Mater. Trans. A. 49 (2018) 3831–3837, https://doi.org/10.1007/s11661-018-4769-y.

[17] A.R. Balachandramurthi, J. Moverare, N. Dixit, D. Deng, R. Pederson, Microstructural influence on fatigue crack propagation during high cycle fatigue testing of additively manufactured Alloy 718, Mater. Charact. 149 (2019) 82–94, https://doi.org/10.1016/j.matchar.2019.01.018.

[18] M.M. Kirka, D.A. Greeley, C. Hawkins, R.R. Dehoff, Effect of anisotropy and texture on the low cycle fatigue behavior of Inconel 718 processed via electron beam melting, Int. J. Fatigue. 105 (2017) 235–243, https://doi.org/10.1016/j.ijfatigue.2017.08.021.

[19] J.W. Yoon, N.Y. Kim, J.H. Kim, J.T. Yeom, N.K. Park, Recrystallization and grain growth during Alloy 718 processing, Mater. Sci. Forum. 539–543 (2007) 3094–3099, https://doi.org/10.4028/www.scientific.net/KEM.345-346.57.

[20] E. Chlebus, K. Gruber, B. Kuźnicka, J. Kurzac, T. Kurzynowski, Effect of heat treatment on microstructure and mechanical properties of Inconel 718 processed by selective laser melting, Mater. Sci. Eng. A. 639 (2015) 647–655, https://doi.org/10.1016/j.msea.2015.05.035.

[21] W.M. Tucho, P. Cuvillier, A. Sjolyst-Kverneland, V. Hansen, Microstructure and hardness studies of Inconel 718 manufactured by selective laser melting before and after solution heat treatment, Mater. Sci. Eng. A. 689 (2017) 220–232, https://doi.org/10.1016/j.msea.2017.02.062.

[22] L.M. Sochalski-Kolbus, E.A. Payzant, P.A. Cornwell, T.R. Watkins, S.S. Babu, R.R. Dehoff, M. Lorenz, O. Ovchinnikova, C. Duty, Comparison of residual stresses in Inconel 718 simple parts made by electron beam melting and direct laser metal sintering, Metall. Mater. Trans. A. 46 (2015) 1419–1432, https://doi.org/10.1007/s11661-014-2722-2.

[23] A.R. Balachandramurthi, J. Olsson, J. Ålgårdh, A. Snis, J. Moverare, R. Pederson, Microstructure tailoring in electron beam powder bed fusion additive manufacturing and its potential consequences, Results Mater. 1 (2019) 100017, https://doi.org/10.1016/j.rinma.2019.100017.

[24] ASTM, F3055 − 14a, Standard Specification for Additive Manufacturing Nickel

Alloy (UNS N07718) With Powder Bed Fusion, West Conshohocken, PA, USA, (2014), https://doi.org/10.1520/F3055-14A.

[25] E. Zaninelli, Effects of Post-processing on EBM Fabricated Inconel 718, Master's thesis University of Modena and Reggio Emilia, Italy, 2018https://morethesis.unimore.it/ETD-db/ETD-relatori/manage_etd.

[26] G.F. Vander Voort, E.P. Manilova, Metallographic techniques for superalloys, Microsc. Microanal. 10 (2004) 690–691, https://doi.org/10.1017/S1431927604883442.

[27] A. Chamanfar, L. Sarrat, M. Jahazi, M. Asadi, A. Weck, A.K. Koul, Microstructural characteristics of forged and heat treated Inconel-718 disks, Mater. Des. 52 (2013) 791–800, https://doi.org/10.1016/j.matdes.2013.06.004.

[28] M.B. Djurdjevič, M.A. Grzinčič, The effect of major alloying elements on the size of secondary dendrite arm spacing in the as-cast Al-Si-Cu alloys, Arch. Foundry Eng. 12 (2012) 19–24, https://doi.org/10.2478/v10266-012-0004-2.

[29] E. Vandersluis, C. Ravindran, Comparison of measurement methods for secondary dendrite arm spacing, Metallogr. Microstruct. Anal. 6 (2017) 89–94, https://doi.org/10.1007/s13632-016-0331-8.

[30] S. Kou, Welding Metallurgy, 2nd edition, Wiley, 2003, https://doi.org/10.1002/0471434027.

[31] A. Mitchell, The precipitation of primary carbides in IN718 and its relation to solidification conditions, Superalloys 718, 625, 706 Deriv., Pittsburgh, USA, 2005, pp. 299–310, , https://doi.org/10.7449/2005/Superalloys_2005_299_310.

[32] M.M. Kirka, K.A. Unocic, N. Raghavan, F. Medina, R.R. Dehoff, S.S. Babu, Microstructure development in electron beam-melted Inconel 718 and associated tensile properties, JOM. 68 (2016) 1012–1020, https://doi.org/10.1007/s11837-016-1812-6.

[33] P. Karimi, E. Sadeghi, P. Åkerfeldt, J. Ålgårdh, J. Andersson, Influence of successive thermal cycling on microstructure evolution of EBM-manufactured alloy 718 in track-by-track and layer-by-layer design, Mater. Des. 160 (2018) 427–441, https://doi.org/10.1016/j.matdes.2018.09.038.

[34] J.K. Tien, T. Caulfield, Superalloys, Supercomposites, and Superceramics, Academic Press, New York, Boston, 1989, https://doi.org/10.1016/C2012-0-01671-7.

[35] W. Kurz, D.J. Fisher, Fundamentals of Solidification, (1992), https://doi.org/10.1002/crat.2170210909.

[36] J. Shao, G. Yu, X. He, S. Li, R. Chen, Y. Zhao, Grain size evolution under different cooling rate in laser additive manufacturing of superalloy, Opt. Laser Technol. 119 (2019) 105662, https://doi.org/10.1016/j.optlastec.2019.105662.

[37] A.T. Polonsky, M.P. Echlin, W.C. Lenthe, R.R. Dehoff, M.M. Kirka, T.M. Pollock, Defects and 3D structural inhomogeneity in electron beam additively manufactured Inconel 718, Mater. Charact. 143 (2018) 171–181, https://doi.org/10.1016/j.matchar.2018.02.020.

[38] F.J. Humphreys, M. Hatherly, Recrystallization and related annealing phenomena, 2nd edition, Elsevier, 2004, https://doi.org/10.1016/B978-0-08-044164-1.X5000-2.

[39] R. Watson, M. Preuss, J.Q. Da Fonseca, T. Witulski, G. Terlinde, M. Büscher, Characterization of abnormal grain coarsening in Alloy 718, MATEC Web Conf. 14 (2014) 07004, , https://doi.org/10.1051/matecconf/20141407004.

[40] N. Bozzolo, A. Agnoli, N. Souai, M. Bernacki, R.E. Loge, Strain induced abnormal grain growth in nickel base superalloys, Mater. Sci. Forum Vol. 753 (2013) 321–324, https://doi.org/10.4028/www.scientific.net/MSF.753.321.

[41] T. Raza, J. Andersson, L.-E.E. Svensson, Varestraint weldability testing of additive manufactured alloy 718, Sci. Technol. Weld. Join. 23 (2018) 606–611, https://doi.org/10.1080/13621718.2018.1437338.

[42] S. Mahajan, C.S. Pande, M.A. Imam, B.B. Rath, Formation of annealing twins in F.C.C. crystals, Acta Mater. 45 (1997) 2633–2638, https://doi.org/10.1016/S1359-6454(96)00336-9.

[43] T. Gladman, On the theory of the effect of precipitate particles on grain growth in metals, Proc. R. Soc. London. Ser. A. Math. Phys. Sci. 294 (1966) 298–309, https://doi.org/10.1098/rspa.1966.0208.

[44] R. Seede, A. Mostafa, V. Brailovski, M. Jahazi, M. Medraj, Microstructural and microhardness evolution from homogenization and hot isostatic pressing on selective laser melted Inconel 718: structure, texture, and phases, J. Manuf. Mater. Process. 2 (2018) 30, https://doi.org/10.3390/jmmp2020030.

[45] J.M. Poole, K.R. Stultz, J.M. Manning, The effect of ingot homogenization practice on the properties of wrought Alloy 718 and structure, in: E.A. Loria (Ed.), Superalloy 718-Metallurgy Appl, The Minerals, Metals & Materials Society, Pittsburgh, USA, 1989, pp. 219–228, , https://doi.org/10.7449/1989/Superalloys_1989_219_228.

[46] R.B. Frank, C.G. Roberts, J. Zhang, Effect of nickel content on delta solvus temperature and mechanical properties of Alloy 718, 7th Int. Symp. Superalloy 718 Deriv, 2010, pp. 725–736, , https://doi.org/10.7449/2010/Superalloys_2010_725_736.

[47] M. Stockinger, E. Kozeschnik, B. Buchmayr, W. Horvath, Modelling of δ-phase dissolution during preheating of Inconel718 turbine disks, Superalloy 718, 625, 706, Var. Deriv, 2001, pp. 141–148, , https://doi.org/10.7449/2001/Superalloys_2001_141_148.

[48] A. Oradei-Basile, J.F.F. Radavich, A current T-T-T diagram for wrought Alloy 718, Superalloys, 1991, pp. 325–335, , https://doi.org/10.7449/1991/superalloys_1991_325_335.

[49] V. Beaubois, J. Huez, S. Coste, O. Brucelle, J. Lacaze, Short term precipitation kinetics of delta phase in strain free Inconel* 718 alloy, Mater. Sci. Technol. 20 (2004) 1019–1026, https://doi.org/10.1179/026708304225019830.

[50] S. Li, J. Zhuang, J. Yang, Q. Deng, J. Du, X. Xie, B. Li, Z. Xu, Z. Cao, Z. Su, C. Jiang, The effect of δ-phase on crack propagation under creep and fatigue conditions in Alloy 718, in: E.A. Loria (Ed.), Superalloys 718, 625, 706 Var. Deriv, The Minerals, Metals & Materials Society, Pittsburgh, PA, USA, 1994, pp. 545–555, , https://doi.org/10.7449/1994/Superalloys_1994_545_555.

[51] L.C.M. Valle, L.S. Araújo, S.B. Gabriel, J. Dille, L.H. de Almeida, The effect of δ phase on the mechanical properties of an Inconel 718 superalloy, J. Mater. Eng. Perform. 22 (2013) 1512–1518, https://doi.org/10.1007/s11665-012-0433-7.

[52] AMS 2774A, Heat Treatment: Wrought Nickel Alloy and Cobalt Alloy Parts, AMS, 2005, https://doi.org/10.4271/AMS2774.

[53] X. You, Y. Tan, S. Shi, J.-M.M. Yang, Y. Wang, J. Li, Q. You, Effect of solution heat treatment on the precipitation behavior and strengthening mechanisms of electron beam smelted Inconel 718 superalloy, Mater. Sci. Eng. A. 689 (2017) 257–268, https://doi.org/10.1016/j.msea.2017.01.093.

[54] M.C. Chaturvedi, Y. Han, Strengthening mechanisms in Inconel 718 superalloy, Met. Sci. 17 (1983) 145–149, https://doi.org/10.1179/030634583790421032.

[55] A. Devaux, L. Nazé, R. Molins, A. Pineau, A. Organista, J.Y. Guédou, J.F. Uginet, P. Héritier, Gamma double prime precipitation kinetic in Alloy 718, Mater. Sci. Eng. A. 486 (2008) 117–122, https://doi.org/10.1016/j.msea.2007.08.046.

[56] J.J. Schirra, D.V. Viens, Metallurgical factors affecting the machinability of Inconel 718, in: E.A. Loria (Ed.), Superalloys 718, 625, 706 Var. Deriv, The Minerals, Metals & Materials Society, 1994, pp. 827–838, , https://doi.org/10.7449/1994/Superalloys_1994_827_838.

[57] F.R. Caliari, K.C.G. Candioto, D.A.P. Reis, A.A. Couto, C. de M. Neto, C.Â. Nunes, Effect of aging treatment on inconel 718 superalloy: application in elevated temperatures, Mater. Sci. Forum. 805 (2015) 199–203, https://doi.org/10.4028/www.scientific.net/MSF.805.199.

[58] A. Niang, B. Viguier, J. Lacaze, Some features of anisothermal solid-state transformations in alloy 718, Mater. Charact. 61 (2010) 525–534, https://doi.org/10.1016/j.matchar.2010.02.011.